On the Voltage Stability and Network Scalability of Onboard DC Microgrids for Hybrid Electric Aircraft

Andrei-Constantin Braitor, Houria Siguerdidjane, Alessio Iovine

On the Voltage Stability and Network Scalability of Onboard DC Microgrids for Hybrid Electric Aircraft

October 28, 2024

Andrei-Constantin Braitor, Member, IEEE, **Houria Siguerdidjane**, Member, IEEE, **Alessio Iovine**, Member, IEEE,

Laboratoire des Signaux et Systèmes (L2S), CentraleSupélec, CNRS, Université Paris-Saclay, Gif-sur-Yvette, France *Corresponding author: Andrei-Constantin Braitor*

{andrei.braitor, houria.siguerdidjane, alessio.iovine}@centralesupelec.fr

Abstract

This paper looks into the voltage stability and network scalability of self-contained converter-based dirrect current (DC) microgrid (MG) under an innovative control approach, namely a nonlinear adaptive droop-based controller with overcurrent protection, devised for hybrid electric aircraft (HEA) applications. Apart from guaranteeing tight voltage regulation and accurate adaptive distribution of load power across parallel batteries proportional with their current state of charge (SoC), the controller features an inherent overcurrent protection. Notably, the applied nonlinear adaptive droop-based controller introduces a virtual voltage and a constant virtual resistance, placed in series with the inductance and parasitic resistance of each DC/DC bidirectional boost converter. Moreover, the voltage stability for the n-dimensional system is subsequently investigated, providing valuable insights into the voltage dynamic behaviour, followed by a network scalability study based on the system's passivity properties. Finally, numerical simulations replicating various in-flight scenarios align with and validate our theoretical developments in the pursuit of minimising emissions, environmental impact, and operational costs.

Index Terms - hybrid electric aircraft, DC microgrids, voltage stability, microgrid scalability, adaptive droop-based control.

Nomenclature

ρ positive constant

σ control state

τ time constant

C converter output capacitance

E_{max} constant virtual voltage

g, R line conductance/ resistance

i_L, i input/ output current

k_P, k_I, k_D constant PID control gains

L converter input inductance

m constant droop coefficient

P active power

r_v dynamic virtual resistance

SOC state of charge

U, V converter input/ output voltage

u converter duty ratio

V^* reference voltage

Y conductance matrix

1 INTRODUCTION

Aircraft electrical networks play a pivotal role in powering various essential components of aircraft, encompassing flight controls, avionics, navigation equipment, communications, lighting systems, and other critical functionalities. The pursuit of minimising emissions, environmental impact, and operational costs throughout the lifespan demands components that exhibit high reliability, reduced overall dimensions, and decreased weight aimed to ensure optimal operational efficiency [1]. Such imperative propels the inclination towards electrifying more subsystems, placing electrical power system (EPS) at the forefront of future aircraft designs that emphasize uninterruptible power supply throughout flight plans [2, 3, 4].

The endeavour to replace conventional hydraulic, mechanical, and pneumatic actuators with electrical components heralds the potential to recalibrate energy utilisation within aircraft. This allows for optimisation during various flight phases and leverages the benefits conferred by aircraft EPS controllers.

Contemporary aircraft models like the Boeing 787 and/ or Airbus A380 feature an increased number of EPS components compared to older counterparts [5, 6], and this trajectory is already anticipated to intensify in the near future. However, as the installed electrical power capacity grows, novel challenges emerge in designing and controlling the aircraft's onboard electrical network.

Amidst this push for electrification, the concept of DC MG emerges as a promising avenue for onboard power distribution systems in the electrical aircraft industry [7]. DC MG offer unparalleled advantages, including heightened efficiency, seamless integration with battery energy storage system (BESS), simple control structures, absence of frequency and reactive power issues, as well as a reduction in direct to alternative current conversion stages [8]. The control complexities associated with onboard DC MG typically involve tasks such as maintaining voltage stability, effectively distributing load power across interconnected sources, ensuring overall system stability, and implementing robust protection mechanisms.

Onboard DC MG, characterised by enhanced reliability and devoid of inter-unit communication, often adopt distributed control strategies where each unit's control method relies on locally available variables. Droop controllers have proven effective in decentralized approaches due to their simplicity, linear nature, and ability to operate without additional communication infrastructure. This inherent modularity, bolstered reliability, and cost reduction have been highlighted in works like [9, 10, 11]. Nonetheless, standard droop-based control introduces a trade-off between load current distribution and output voltage regulation, particularly pronounced under substantial load demands. To mitigate this, one common practice to restore voltage and enhance power sharing is to utilise a secondary controller, as seen in [12]. Consensus-based and improved droop techniques have been explored in [13] and [14] respectively, incorporating methods that use compensation terms for voltage augmentation or consensus algorithms for power sharing assurance. Other variations of droop controllers have been proposed in [15, 16, 17], while SoC-based adaptive droop techniques for MG that integrate BESS have been extensively documented in [18, 19].

Beyond ensuring microgrid reliability, the quest for safe and secure operation devoid of extra protection mechanisms, like fuses and/ or circuit breakers, has gained traction as a significant research avenue [20]. While certain methods have been put forth to address this aspect (e.g., [21]), it remains an ongoing research challenge. A related aspect of protection concerns constant power load (CPL), which are represented in the aircraft's EPS by closely regulated motors and downstream converters. They present challenges that emanate from their influence on load-side power conditioning. Their nonlinear characteristics further cause them to act similar to negative impedances in small-signal analyses [22]. In light of these intricacies, the existence of a stable steady-state behaviour becomes pivotal for the safe and dependable operation of the onboard DC MG. However, addressing this issue analytically proves intricate and has posed numerous challenges in the past.

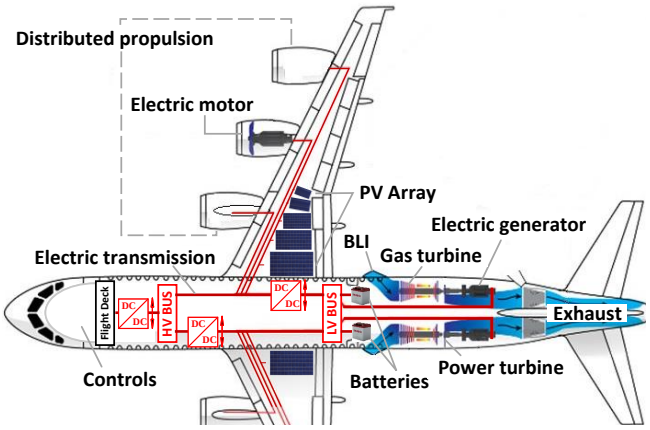

Figure 1: Concept diagram of an onboard DC microgrid of an HEA

In the realm of EPS, the concept of network scalability has emerged as a critical consideration, particularly in the context of onboard DC MG for HEA. The ability to seamlessly incorporate and disengage power sources within these microgrids is of paramount importance for enhancing their adaptability and resilience. Of particular interest is the property of passivity, which holds the potential to ameliorate voltage stability concerns during source connections and disconnections. Passivity, often associated with control strategies for ensuring network scalability, is an area of noteworthy focus. Recent research endeavours such as [23, 24] have delved into diverse facets of network scalability, encompassing passivity control and its ramifications on voltage stability within DC microgrids. These studies provide valuable insights for the development of scalable and passively controlled onboard DC MG tailored to the future requirements of hybrid electric aircraft.

The present study drew inspiration from the aim to investigative electrical aircraft design concepts that incorporate BESS and leverage solar energy via solar cells for electricity generation. While solar-powered aircraft have predominantly been engineered for low-altitude high-endurance (LAHE) aircraft concepts, as seen in [25], the introduction of an adaptive droop-based control technique to ensure precise voltage control and SoC-dependent load power distribution, along with a current-limiting capability, appears novel and unexplored within the current research landscape.

The present research work builds upon and extends our already proposed controller in [11] by introducing several noteworthy advancements:

1. the cornerstone of our adaptive droop controller lies in the introduction of a unified approach that integrates an adaptive droop-based controller for BESS. This innovative controller design draws its cues from the real-time state of charge of individual BESS units. Compared to the initial paper, a clear advantage highlighted in this newly proposed work is the numerical showcase of the inherent overcurrent protection it provides.

2. to expand the research scope, we delve into a thorough analysis of voltage stability. Relying on the

foundation of the unified adaptive droop controller, we probe into the intricacies of the system's voltage stability properties. An extended analysis offers insights into how the proposed controller influences voltage stability under various in-flight operational conditions.

3. another novel endeavour is the exploration of microgrid scalability. Leveraging the capabilities of the controller, we embark on a comprehensive investigation into the dynamics of microgrid expansion. This analysis assesses how the proposed controller adapts to the integration of additional energy sources within the microgrid. By scrutinising the behaviour of the system as it grows, we uncover insights into its scalability limits and identify strategies to ensure stable and efficient operation.

4. to validate and substantiate the effectiveness of our theoretical developments, we subject them to rigorous simulation tests conducted under realistic in-flight conditions. Performed tests incorporate actual global horizontal irradiance (GHI) data, which accurately reflects the variable solar energy input experienced by the photovoltaic (PV) arrays positioned on aircraft wings during flight. The performance of our proposed controller is validated through an exhaustive testing scenario that emulates the influence of in-flight manoeuvrers on the onboard EPS.

The subsequent structure of the paper is organized as follows: Section 2 presents the microgrid model and network configuration, incorporating CPL linked to the low-voltage bus. The primary control design, along with pertinent technical considerations, is proposed in Section 3, followed by an exploration of voltage stability in Section 4 and microgrid scalability in Section 5. Onboard microgrid numerical simulation outcomes are detailed in Section 6, while Section 7 encapsulates concluding remarks and insights drawn from our study.

2 Onboard DC Microgrid Model for HEA

Illustrated in Fig. 1, there is a common topology of an onboard DC MG within an HEA. More details on the aircraft's design can be found here [26]. This configuration comprises two main buses, a high-voltage (HV) and a low-voltage (LV), interconnected through a bidirectional converter to facilitate dual-direction power transfer. Both buses accommodate an array of energy sources and/ or BESS linked in parallel, coupled with various loads. An electrical representation of this dual-bus system setup is showcased in Fig. 2. Distributed propulsion encompasses a range of propulsion methods employed within the HEA. Note that BESS are depicted as controllable voltage sources denoted as $U_{1...n}$, connected via two-way boost converters to the LV bus. Within each converter's input, $r_{s,j}$ and L_j symbolise the parasitic resistance and inductor, whereas C_j and g_j denote the output capacitor and line conductance, respectively, with the index $j = \{1, \ldots, n, HV\}$. Notably, the LV bus is equipped with a constant

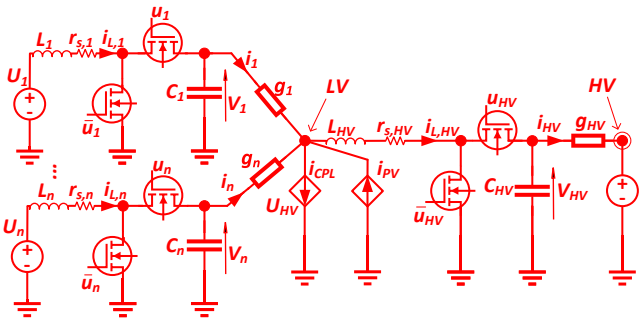

Figure 2: Dual-bus electrical circuit of the onboard DC microgrid

power load, manifesting as a current source labelled i_{CPL}, and akin to this, the PV array denoted as $i_{PV} = f\,(GHI)$.

Utilising Kirchhoff's laws, we can formulate the current and voltage dynamics for each converter at the LV bus as

$$L_j \frac{di_{L,j}}{dt} = U_j - r_{s,j} i_{L,j} - (1 - u_j)\, V_j \tag{1}$$

$$C_j \frac{dV_j}{dt} = (1 - u_j)\, i_{L,j} - i_j \tag{2}$$

with $j \in \{1, \ldots, n, HV\}$, where $i_{L,j}$, i_j and V_j represent the input and output current, and capacitor voltage, respectively. Note that u_j is the duty-ratio, belonging to the closed set $u_j \in [0, 1]$.

The expression for the CPL at the LV bus is given by the power balance equation, i.e.,

$$P = i_{CPL} U_{HV} \tag{3}$$

with constant P being the CPL power, whilst i_{CPL}, the load current, equal to the sum of all currents at the low-voltage bus as shown below

$$i_{CPL} = i_{PV} + i_{L,HV} + \sum_{i=1}^{n} g_i\,(V_i - U_{HV})\,, \tag{4}$$

with $i \in \{1, \ldots, n\}$. The voltage solutions U_{HV} in the presence of CPL are extensively documented, favouring the higher voltage solution as the viable option. Additional insights into the existence and uniqueness of these feasible solutions are elaborated upon in [27, 28]. A comprehensive discussion on voltage stability is slated for Section V, particularly emphasizing the interrelation/ dependence between voltage and power reliability.

3 Control Design

Within this section, we put forth a cohesive strategy that integrates the adaptive droop-based controller into the nonlinear state-limiting proportional integral derivative (sl-PID) control structure.

Proposition 1. *Consider the output of the nonlinear sl-PID, equal to the control input u_i of a plant, being*

$$u_i = -k_{P,i}x_i + M_i \int k_{I,i}\left(r_i - h_i\left(x_i\right)\right) cos\left(\sigma_i\right) - k_{D,i}\frac{\partial h_i}{\partial x_i}\dot{x}_i$$

where $M_i, k_{P.i}, k_{I,i} > 0$, $k_{D,i} \geq 0$. For a zero initial condition of the integral state σ_i, the control state remains within $\sigma_i\left(t\right) \in \left[-\frac{\pi}{2}, \frac{\pi}{2}\right]$, $\forall\, t \geq 0$. Anytime $\sigma_i\left(t\right) \to \pm\frac{\pi}{2}$, $\dot{\sigma}_i \to 0$, meaning σ_i will converge to the lower or upper limit $\left(\pm\frac{\pi}{2}\right)$ independently of the term $r_i - h\left(x_i\right)$.

Proof. is presented in the sl-PID developed in [29].

We present a decentralised control strategy aimed at attaining voltage regulation at individual voltage buses and facilitating power sharing among parallel sources without the need for communication, achieved through a droop-based approach. However, due to the limitations of conventional droop control when confronted with disparate output impedances introduced by individual converters, a standard solution is to implement a robust droop-based approach as outlined in [30]. Therein, the droop equation becomes, when considering converters interfacing BESS, as

$$\tau_i \dot{V}_i = V^* - U_{HV} - \frac{m_i}{SOC_i^{\rho}} i_i. \tag{5}$$

Here, SOC_i is the state of charge of the i-th battery-unit, ρ stands as a positive constant, i.e. $\rho \in \mathbb{N}$, m_i pertains to the power capacity of the battery, whilst τ_i is a time-constant (in seconds).

Under steady-state conditions, the subsequent relationship emerges:

$$\frac{m_1}{SOC_1^{\rho}} i_1 = \frac{m_2}{SOC_2^{\rho}} i_2 = \cdots = \frac{m_n}{SOC_n^{\rho}} i_n. \tag{6}$$

Furthermore, in cases where uniform power capacity is assumed for each battery, having $m_1 = m_2 = \cdots = m_n$, power sharing occurs in proportion to their individual SoC $\frac{1}{SOC_1^{\rho}} i_1 = \frac{1}{SOC_2^{\rho}} i_2 = \cdots = \frac{1}{SOC_n^{\rho}} i_n$, resulting in the battery with the highest state of charge injecting more power into the network. However, it is important to note that batteries reaching the same SoC contribute the same amount of power to the system, which holds true during charging cycles as well.

Regarding the converter in-between the LV and HV buses, the droop is modified and takes the form:

$$\tau \dot{V}_{HV} = V^* - V_{HV} - m\left(i_{HV} - i_{set}\right), \tag{7}$$

where τ is, same as before, a time-constant (in seconds), and i_{set} acts as a set-current reference

determining the current magnitude transferred from the HV to the LV bus. Notably, when $i_{set} < 0$, the power direction shifts, going from the LV to the HV bus.

Note that the introduction of droop controllers introduces voltage discrepancies that consequently impact current sharing accuracy. This phenomenon, known as *circulating currents between converters*, is addressed to ensure effective operation of parallel-operated sources. In the context of two BESS units located at the low-voltage bus, the circulating current i_{cc} becomes

$$i_{cc} = i_1 - \frac{m_2}{SOC_2^{\rho}} \left(\frac{m_1}{SOC_1^{\rho}} \right)^{-1} i_2. \tag{8}$$

However, due to the application of the robust droop-based approach and the satisfaction of equality (6), the circulating current ultimately tends toward zero, i.e., $i_{cc} \to 0$.

Now, let us introduce the duty ratio as the control input, implemented as shown below

$$u_j = 1 - \frac{U_j - E_{max,j} \sin(\sigma_j) + r_{v,j} i_{L,j}}{V_j}. \tag{9}$$

Here, σ_j follows the dynamics of the nonlinear sl-PID presented in [29], specified as

$$\dot{\sigma}_j = \frac{kI,j}{r_{v,j}} \phi(i_{L,j}, V_j) \cos(\sigma_j) \tag{10}$$

where function $\phi(\cdot)$ takes different forms for converter-interfaced units, denoted as

$$\phi(i_{L,j}, V_j) = \begin{cases} equation\,(5), & \forall\ j \in \{1, \ldots, n\} \\ equation\,(7), & interlinking\ converter \end{cases}$$

For a better understanding, the control structure diagram is included in Fig. 3. One assumes that, at the LV bus, at least one converter-interfaced source is connected to stabilise the bus voltage, which is both reasonable and non-restrictive, particularly in the context of islanded MG, such as the self-contained onboard DC MG studied in this work.

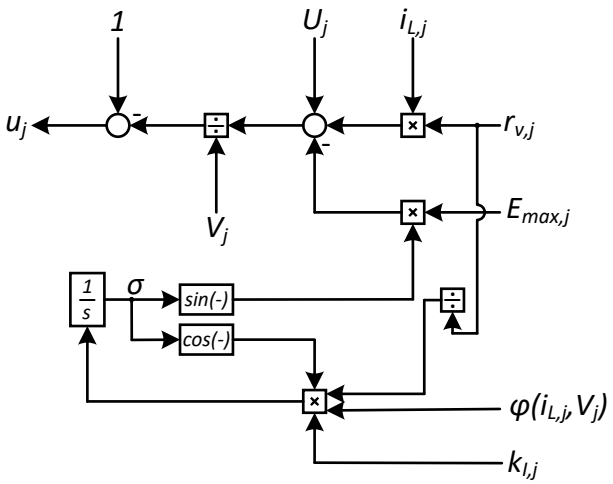

Figure 3: Control structure diagram implementation

When substituting the control input u_j from (9) into the open-loop current dynamics (1), the closed-loop current dynamics are derived as follows:

$$L_j \frac{di_{L,j}}{dt} = E_{max,j} \sin(\sigma_j) - (r_{s,j} + r_{v,j})\, i_{L.j} \tag{11}$$

In this equation, $E_{max,j} \sin(\sigma_j)$ represents a virtual voltage, and $r_{v,j}$ signifies a constant virtual resistance in series with $r_{s,j}$. Due to the negligible value of $r_{s,j}$ compared to the virtual resistance (i.e., $r_{s.j} << r_{v,j}$), it follows that at steady state $i_{L,j} \approx \frac{E_j \sin(\sigma_j)}{r_{v,j}}$. The subsequent proposition ensures current limitation.

Proposition 2. *The solutions $i_{L,j}(t)$ of (11) are uniformly ultimately bounded, i.e., $|i_{L,j}(t)| < i_{L,i}^{max}$ for all $t \geq 0$, with the maximum currents being $i_{L,j}^{max} = \frac{E_{max.j}}{r_{v,j}}$.*

Proof. follows similarly as in [11, Prop. 2].

The approach maintains two-way current limitation. One notices from controller dynamics (10) and closed-loop dynamics (11), that when $\phi(i_{L,j}, V_j) = 0$, then $\sigma_j = \sigma_{j,e}$, and the inductor current value takes the form

$$i_{L,je} = \frac{E_{max,j} \sin(\sigma_{j,e})}{r_{v,j}}. \tag{12}$$

As $\sigma_{j,e} \in \left[-\frac{\pi}{2}, \frac{\pi}{2}\right]$, the inductor current could be positive or negative, guaranteeing two-way power-flow operation. When $\sigma_{j,e} = -\frac{\pi}{2}$, $i_{L,je} = -\frac{E_{max,j}}{r_{v,j}} = -i_{L,j}^{max}$, corresponding to overcurrent protection in both directions of power flow.

Different from conventional overcurrent protection control schemes, this approach mathematically guarantees an upper bound for the inductor current even during transients, without requiring limiters or saturation units. The proposed controller is slowing down near its imposed limits preventing integrator wind-up that could introduce instability.

4 Voltage stability

Voltage stability plays a crucial role in electric aircraft applications, as highlighted in research works such as [28]. Thus, the existence of a steady-state behaviour, characterised by voltage equilibria, holds immense significance for ensuring a secure and dependable operation of DC MG incorporating CPL.

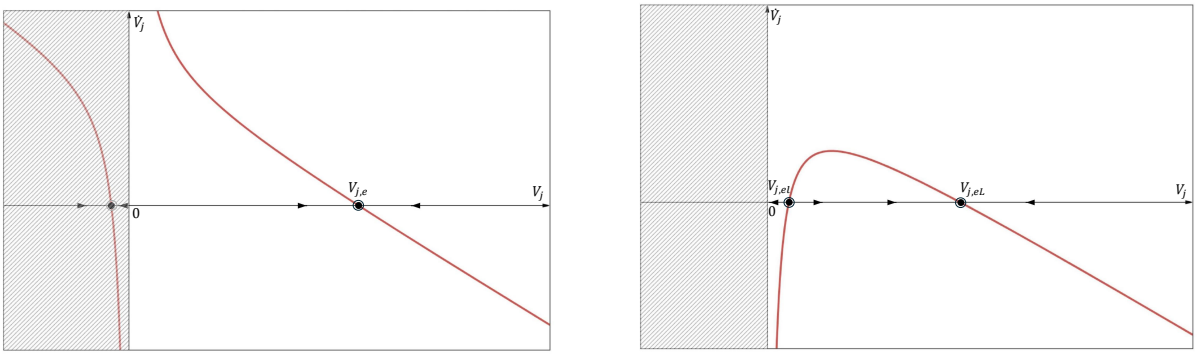

Figure 4: Phase portrait of voltage dynamics (14) for positive (left) and negative (right) power

It is well understood that an increase in CPL power leads to a voltage drop in the CPL voltage U_{HV}. In response, the current increases to fulfil the power demand. However, when the system lacks proper control mechanisms to prevent the voltage from dropping below the stable point's voltage level, it may continue to decrease until reaching zero. Simultaneously, the current will tend towards infinity. This means that CPL introduce power conditioning on the load side. The nonlinear characteristics introduced into the power balance equation can potentially trigger voltage collapse [31] when the requested power exceeds a certain threshold.

To avert voltage collapse, a condition for choosing a set-voltage reference, V^*, can be implemented. Various conditions have been proposed in the literature, as seen in works like [27, 28]. These conditions generally follow a common rule, encapsulated by an inequality such as

$$V^* > 2\sqrt{YP}, \tag{13}$$

which essentially dictates that the reference voltage, in broader terms, must exceed a function linked to the microgrid network Y and the CPL power P.

To delve deeper into these implications, it is essential to examine the behaviour of the voltage dynamics. Substituting the control input u_j into equation (2) yields the closed-loop voltage dynamics

$$C_j\dot{V}_j = -\frac{P_j}{V_j} + \frac{U_j i_{L,j} - E_{max,j}\sin\sigma_j i_{L,j} + r_{v,j} i_{L,j}^2}{V_j}. \tag{14}$$

Notice that the power supplied/ received by each converter j is $P_j = U_j i_{L,j}$ since at steady state, according to equation (12), the following equality takes place $E_{max} \sin \sigma i_L = r_v i_L^2$. It is important to note that power P_j can exhibit both positive and negative values. Depending on the sign of the power, one can formulate the following proposition to ensure closed-loop voltage stability. A similar techniques has been employed in [32, Prop.5.8], however, it falls short in delivering the requisite depth of insight, by lacking the critical discussion and practical applicability, which the following proposition aims to achieve.

Proposition 3. *When inequality* (13) *is fulfilled, for both charging ($P_j < 0$) and discharging ($P_j > 0$) scenarios, the following conditions arise:*

- *In the case of $P_j > 0$, the voltage exhibits a single stable equilibrium point.*
- *In scenarios where $P_j < 0$, the voltage experiences two equilibrium points — one stable and one unstable.*
- *For instances where $P_j = 0$, the voltage dynamics manifest as a linear asymptotically stable dynamic system.*

Proof. Inequality (13) becomes both a necessary and sufficient condition for the presence of a voltage equilibrium. Then, the proof becomes straightforward by considering that $V_j > 0$ and examining the phase-portrait plots for the right-hand side of the closed-loop voltage dynamics under positive and negative power, as shown in Fig. 4.

Moreover, for $P_j < 0$, an intriguing phenomenon arises when inequality (13) is not strictly adhered to, meaning $V^* \geq 2\sqrt{YP}$. Namely, when the inequality becomes an equality $V^* = 2\sqrt{YP}$, the two equilibrium points merge into a singular half-stable fixed point. This leads to a bifurcation event, resulting in a *saddle-node bifurcation* phenomenon. This concludes the proof. □

5 Microgrid Scalability

To achieve system scalability, a critical consideration involves investigating the passivity property when a converter is connected/disconnected. Assuming, for example, that a converter is plugged in/out to the network while in operation, the assessment of the system's passivity becomes paramount. Let us define the system input as $u = V_{n+1} - U_{HV,e}$, and system output as $y = i_{n+1}$, representing the output voltage and output current, of the newly connected $n+1$-th converter-unit. With this configuration, as the network structure undergoes a change, the MG's output current vector encompassing the operating

n converter-units takes the following expression

$$i = Y' \begin{bmatrix} \tilde{V}_1 \\ \vdots \\ u \end{bmatrix} = \underbrace{g\left(I_n - \mathbf{1}_{n\times n} D'\right)}_{\gamma} \tilde{V} + g \left(\mathbf{1}_n - \begin{bmatrix} \frac{\partial \tilde{U}_{HV}}{\partial u} \\ \vdots \\ \frac{\partial \tilde{U}_{HV}}{\partial u} \end{bmatrix} \right) u, \tag{15}$$

where $g = diag\{\frac{1}{R_i}\}$, matrix Y' is the augmented conductance matrix of size n-by-$n+1$, whereas the diagonal matrix D' is intrinsically related to the CPL, having on its main diagonal the elements representing the constant power load resistance of the form $\frac{V_i^2}{P}$. More on this formulation can be found in [33]. Here, $\tilde{U}_{HV} = U_{HV} - U_{HV,e}$ and has the following expression

$$\tilde{U}_{HV} = \begin{bmatrix} \frac{\partial \tilde{U}_{HV}}{\partial \tilde{V}_1} & \dots & \frac{\partial \tilde{U}_{HV}}{\partial \tilde{V}_n} \end{bmatrix} \tilde{V} + \frac{\partial \tilde{U}_{HV}}{\partial u} u.$$

Moving forward, let us consider the vector state as $x = \begin{bmatrix} x_1^T & x_2^T & x_3^T \end{bmatrix}^T$, where $x_1 = i_L - i_{Le}$, $x_2 = V - V_e$, and $x_3 = \sigma - \sigma_e$. This allows us to express the plant system as follows

$$\dot{x} = \mathbf{A}x + \mathbf{B}u \tag{16}$$

$$y = \mathbf{C}x + \mathbf{D} \tag{17}$$

Proposition 4. *The above system is passive given the following Schur complement inequality holds*

$$\left(\mathbf{A}^T P + P\mathbf{A}\right) + \left(P\mathbf{B} - \mathbf{C}^T\right)\left(\mathbf{D}^T + \mathbf{D}\right)^{-1}\left(\mathbf{B}^T P - \mathbf{C}\right) \prec 0 \tag{18}$$

Proof. Here, $\mathbf{D}$ is scalar $\mathbf{D} = g_{n-1}\left(\frac{\partial \tilde{U}_{HV}}{\partial u} - 1\right) < 0$. By employing a similar time-scale separation approach, one can derive the boundary layer system similar to [33], and consequently, the reduced system, which possesses a corresponding Jacobian matrix of the form

$$J = -C^{-1}\left[V_e\right]^{-2}\left(U\left[i_L\right] \pm E_{max}\left[i_L\right] + r_v\left[i_L\right]^2\right) - C^{-1}\gamma. \tag{19}$$

with $[U] = diag\{U_i\}$, $[i_L] = diag\{i_{L,i}\}$, $E_{max} = diag\{E_{max,i}\}$, $r_v = diag\{r_{v,i}\}$. Note that one knows from Section IV that $E_{max}\left[i_L\right] = r_v\left[i_L\right]^2$. It is worth noting that $\gamma \succ 0$ [33], which leads to J being Hurwitz since both terms in the sum are negative-definite matrices.

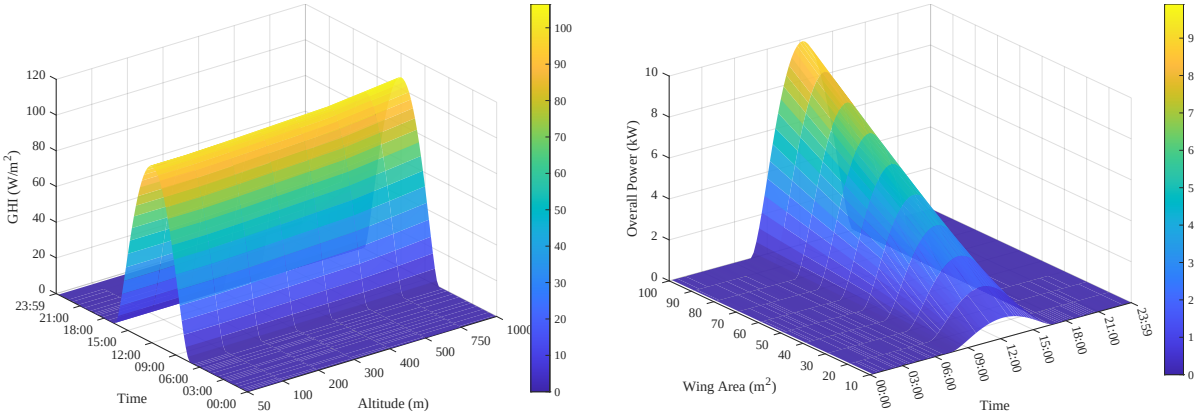

a) b)

Figure 5: a) 24-hour GHI profiles on a sunny day in April at different altitude levels; b) Solar power (in kW) produced at $1000\,m$ altitude depending on aircraft wing area

The Hurwitz property of matrix $\mathbf{A}$ implies the existence of a positive definite matrix $P = P^T \succ 0$, such that $\mathbf{A}^T P + P\mathbf{A} \prec 0$. According to [34, Th.1], the system can be deemed passive if the following Schur complement inequality holds:

$$\left(\mathbf{A}^T P + P\mathbf{A}\right) + \left(P\mathbf{B} - \mathbf{C}^T\right)\left(\mathbf{D}^T + \mathbf{D}\right)^{-1}\left(\mathbf{B}^T P - \mathbf{C}\right) \prec 0 \tag{20}$$

The scalar $\left(\mathbf{D}^T + \mathbf{D}\right)^{-1}$ is negative, allowing to be placed to the front of the expression and multiplied by a term resembling the form $v^T v \succeq 0$, with $v = \mathbf{B}^T P - \mathbf{C}$. This manipulation results in the inequality's second term being negative semi-definite. Given that both terms are Hermitian, with one being strictly negative-definite and the other being negative semi-definite, their sum is invariably strictly negative-definite. This satisfies (20), hence confirming the passivity property in line with [34, Th.1].

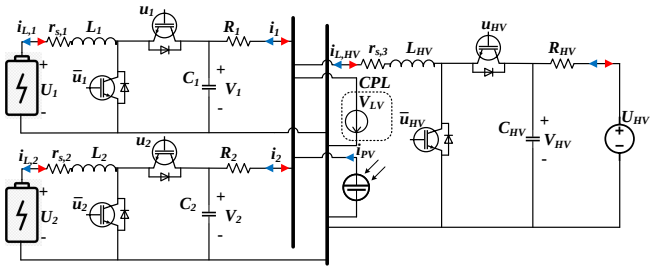

Figure 6: Electrical schematic of the onboard DC MG used for simulation testing

6 Onboard microgrid simulation

In this section, the proposed aircraft EPS concept involves the integration of PV arrays onto the wings of the aircraft, contributing power to the LV bus. Notably, the irradiance received by these panels is inherently influenced by the altitude of the aircraft. Leveraging resources from HelioClim archives and Solar Radiation Data (SoDa) database [35], one can discern a proportionality between the SoDa and aircraft altitude, considering a specified location in Central Europe. This is illustrated in Fig. 5a, where it is evident that the GHI value rises in tandem with increased altitude levels. Similarly, the electrical power injected by the PV arrays increases with a larger wingspan of the aircraft (Fig. 5b).

For the sake of simulations, the conversion of GHI into electrical power is achieved using mathematical formulations akin to those in [36]. The MG under examination is depicted in Fig. 6, and its corresponding parameters are detailed in Table 1. The principal objective here is to evaluate the controller's performance while accomplishing several key tasks: maintaining the LV bus voltage in proximity to the reference value $V^* = 540\,V$, equitably distributing power among the battery-units in proportion to their instantaneous SoC, and ensuring an upper limit for the input currents of all converter-units. Importantly, the adoption of the proposed control methodology within the EPS framework offers the potential to achieve additional goals in the process of electrification, i.e., i) reducing the weight and volume of subsystems, ii) enhancing reliability and ease of maintenance, iii) minimizing environmental impact, iv) optimizing modularity and EPS efficiency, and v) allowing adoption of innovative functionalities and efficient technology.

Table 1: Control and system parameters

Parameter	Value
$r_{s,1},\ r_{s,2},\ r_{s,3}$	$0.001\,\Omega$
$R_1,\ R_2,\ R_{HV}$	$0.22\,\Omega,\ 0.16\,\Omega,\ 0.01\,\Omega$
$C_1,\ C_2,\ C_{HV}$	$100\,\mu F$
$L_1,\ L_2,\ L_{HV}$	$0.002\,H$
$U_1,\ U_2$	$200\,V$
$k_{I1},\ k_{I2},\ k_{I3}$	$0.06,\ 0.03,\ 0.005$
$i_{L,1}^{max},\ i_{L,2}^{max},\ i_{L,HV}^{max}$	$7\,A,\ 7\,A,\ 2\,A$
$r_{v,1},\ r_{v,2},\ r_{v,3}$	$1\,\Omega$

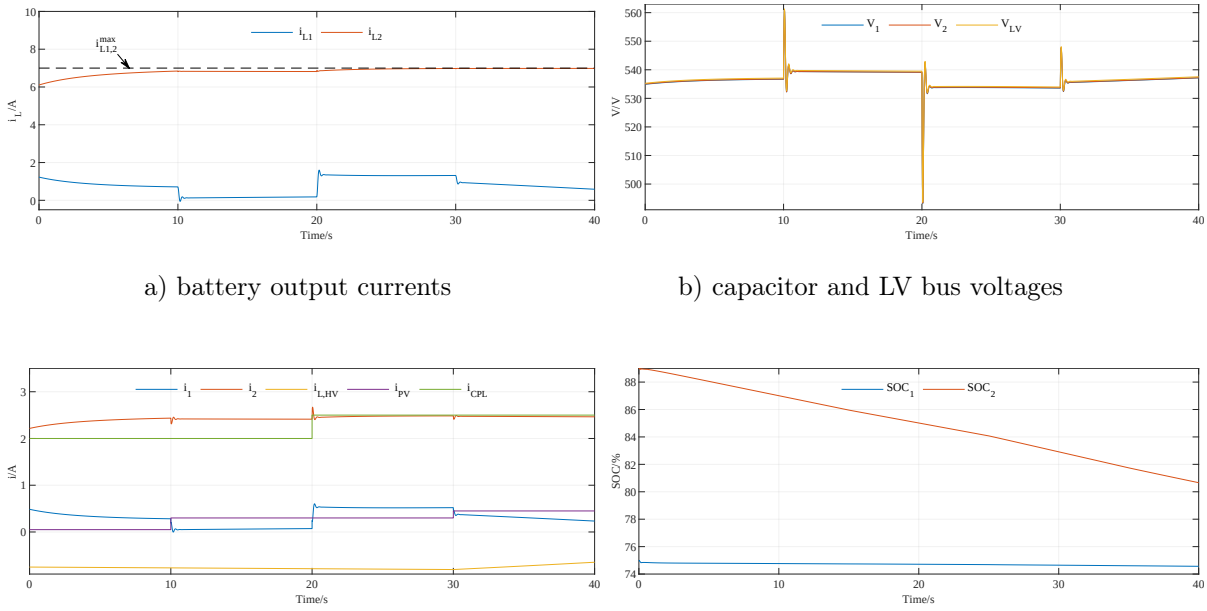

a) battery output currents

b) capacitor and LV bus voltages

c) currents at the LV bus

d) batteries state of charge

Figure 7: DC MG's dynamic response

As presented in Fig. 7, the in-flight simulations encompass a comprehensive testing scenario as outlined below. Initially, the batteries commence with an SoC of 75% and 89%, respectively. During the first $10\,s$, both BESS and the PV system contribute power to the load at the low-voltage bus. Additionally, a small amount of power is being transferred from the HV bus to the LV bus (as depicted in Fig. 7c). Fig. 7a illustrates that the second battery delivers more power compared to the first due to its higher state of charge, and given the large constant $\rho = 8$. As per the theoretical framework developed, the batteries' SoC is expected to converge to one another and then to zero within a finite time (Fig. 7d). The LV bus voltages are meticulously regulated in proximity to the set voltage value, V^* (see Fig. 7b).

Then, at $t = 10\,s$, the power injected by the PV escalates, as evident in Fig. 7c, and the PV current i_{PV} experiences an increase, potentially attributed to an elevation in aircraft altitude. As indicated in Fig. 7c, second battery current and the HV drawn current decrease, unlike the first battery current that slowly increases, while the LV bus voltage promptly reverts to the proximity of the reference value following a short transient period (Fig. 7b). Given the microgrid has a superconductive network with very snall line resistance, there is effectively no voltage drop on the lines. Thus, the voltages at the common bus are almost the same. Importantly, all currents at the LV bus stay below their specified set limits.

A 25% increase in the LV bus power demand occurs at $t = 20\,s$, linked to an augmentation in the usage of onboard instrumentation components. To accommodate this heightened load requirement, both

the batteries and the HV bus augment their power contributions, as one can see in Fig. 7c. The second battery current hits the limit, i.e., $i_{L,2} = i_{L1,2}^{max} = 7\,A$ (Fig. 7a). Note that no violation of the limit occurs. Also, subsequent to a transient undershoot of less than 8%, the voltages rebound to their initial values in proximity to V^*, as illustrated in Fig. 7b.

As one can notice in Fig. 7c, the power injected by the PV arrays increase further at $t = 30\,s$, while also the power from the HV to LV bus slowly ramps up as the control value i_{set} associated with the converter interconnecting the two buses gradually increases. The current limitation for the second battery remains in place (Fig. 7a), while the voltages slowly recover closer to their set reference V^* (Fig. 7b).

Given the simulation is allowed to run for several minutes, the SoC in Fig. 7d of the two batteries will exhibit a diminishing trend and, as anticipated, ultimately converge to zero, demonstrating that the batteries eventually attain the same SoC. The pace of this convergence can be accelerated by manipulating the control parameter ρ in equation (6). For this simulation test ρ has been fixed at value 8.

6.1 Voltage stability

To study the voltage stability, we subject our system to a series of increased load power demands to study the voltage collapse point and the condition in equation (13). More specifically, at $t = 5\,s$, and then every five seconds, the load power demand surges aggressively. It is important to mention that in order to perform this test, one has to increase the current limits to allow the voltage to collapse. The results can be observed in Fig. 8.

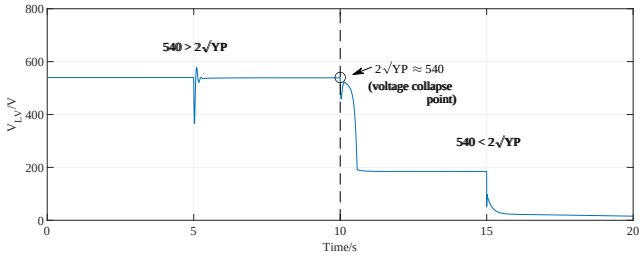

Figure 8: Voltage dynamic response

At $t = 5\,s$, the load power demand increases by 400%. The voltage stability is still kept since inequality (13) is satisfied[1]. The voltage is then tested around the point where the inequality becomes an equality at $t = 10\,s$. The voltage then collapses at the low-voltage solution. Following a final load increase at $t = 15\,s$, the voltage eventually collapses to zero.

[1]The condition in equation (13) can be easily checked, given the conductance matrix Y can be obtained using the line resistance from Table 1, P is the power of the constant power load and V^* is the voltage reference fixed at $540\,V$.

7 Conclusion

This study focuses on investigating the voltage stability and microgrid scalability achieved through the implementation of an adaptive droop controller with integrated current limitation for BESS in onboard DC microgrids designed for HEA. The developed approach harnesses nonlinear control theory to establish a rigorous analytical assurance of the ultimate current bound, thereby ensuring precise voltage regulation and effective load power distribution. The efficacy of the strategy has been successfully demonstrated by establishing voltage stability and conducting thorough microgrid scalability assessments. Rigorous simulation testing has been performed to validate the proposed methodology. These advancements in the design and deployment of EPS control mechanisms are pivotal prerequisites for sustaining the ongoing trend of electrification. The end goal is for these efforts to open the door for the potential to reduce fuel consumption, emissions, and overall operational costs, ultimately contributing to a greener and more economically efficient aviation landscape.

References

[1] Bright Appiah Adu-Gyamfi and Clara Good. Electric aviation: A review of concepts and enabling technologies. *Transportation Engineering*, 9:100134, 2022.

[2] Xavier Roboam, Bruno Sareni, and Andre De Andrade. More electricity in the air: Toward optimized electrical networks embedded in more-electrical aircraft. *IEEE Industrial Electronics Magazine*, 6(4):6–17, 2012.

[3] Pat Wheeler and Sergei Bozhko. The more electric aircraft: Technology and challenges. *IEEE Electrification Magazine*, 2(4):6–12, 2014.

[4] Zhaoyang Zuo, Navid Vafamand, Saleh Mobayen, and Tomislav Dragičević. Finite-time tracking control with fast reaching condition for disturbed more electric aircraft direct current microgrid with constant power loads. *IEEE Transactions on Aerospace and Electronic Systems*, pages 1–10, 2023.

[5] Gerard H. Gaynor. *Boeing and the 787 Dreamliner*, pages 187–218. Wiley-IEEE Press, 2015.

[6] Timo Steinbauer, Gerd Leiprecht, and William Havranek. High performance hil real time for the airbus a380 electrical backup hydraulic actuators. In *2004 Mini Symposia UKACC Control*, pages 71–74, 2004.

[7] Cheng Qiu, Hangyu Li, Zhenkun Song, Jing Huang, Lu Feng, and Xiangyang Wang. Interactional influence analysis of dc bus voltage versus servo systems and stabilization technology for aerospace combined power supply systems. *IEEE Transactions on Aerospace and Electronic Systems*, 59(2):886–896, 2023.

[8] Xin Jin, Yang Shen, and Quan Zhou. A systematic review of robust control strategies in dc microgrids. *The Electricity Journal*, 35(5):107125, 2022.

[9] A-C. Braitor, A.R. Mills, V. Kadirkamanathan, G.C. Konstantopoulos, P.J. Norman, and C.E. Jones. Control of dc power distribution system of a hybrid electric aircraft with inherent overcurrent protection. In *2018 IEEE International Conference on Electrical Systems for Aircraft, Railway, Ship Propulsion and Road Vehicles & International Transportation Electrification Conference (ESARS-ITEC)*, pages 1–6, 2018.

[10] Habibu Hussaini, Tao Yang, Ge Bai, Matías Urrutia-Ortiz, and Serhiy Bozhko. Artificial intelligence-based hierarchical control design for current sharing and voltage restoration in dc microgrid of the more electric aircraft. *IEEE Transactions on Transportation Electrification*, pages 1–1, 2023.

[11] Andrei-Constantin Braitor, Houria Siguerdidjane, and Alessio Iovine. Adaptive droop control design with overcurrent protection for onboard dc microgrids in hybrid electric aircrafts. *IFAC-PapersOnLine*, 55(22):165–170, 2022. 22nd IFAC Symposium on Automatic Control in Aerospace ACA 2022.

[12] Zhangjie Liu, Mei Su, Yao Sun, Hua Han, Xiaochao Hou, and Josep M. Guerrero. Stability analysis of dc microgrids with constant power load under distributed control methods. *Automatica*, 90:62 – 72, 2018.

[13] M.K. Behera, L.C. Saikia, S.K. Ramoji, B. Dekaraja, and S.K. Bhagat. A novel decentralized fo voltage and current control scheme for voltage and frequency regulation in inverter dominated islanded microgrids using improved droop control. *IFAC-PapersOnLine*, 55(1):679–684, 2022.

[14] Xiaomeng Zhang, Xiongchao Yang, Yang Han, Ping Yang, and Amr S. Zalhaf. Consensus enhanced droop control strategy for islanding mode multi converter system. *Energy Reports*, 8:301–309, 2022.

[15] P. H. Huang, P. C. Liu, W. Xiao, and M. S. El Moursi. A novel droop-based average voltage sharing control strategy for DC microgrids. *IEEE Transactions on Smart Grid*, 6(3):1096–1106, May 2015.

[16] F. Cingoz, A. Elrayyah, and Y. Sozer. Plug-and-play nonlinear droop construction scheme to optimize islanded microgrid operations. *IEEE Transactions on Power Electronics*, 32(4):2743–2756, April 2017.

[17] Miguel Jiménez Carrizosa, Alessio Iovine, Gilney Damm, and Pedro Alou. Droop-inspired nonlinear control of a dc microgrid for integration of electrical mobility providing ancillary services to the ac main grid. *IEEE Transactions on Smart Grid*, 13(5):4113–4122, 2022.

[18] Y. A. I. Mohamed and E. F. El-Saadany. Adaptive decentralized droop controller to preserve power sharing stability of paralleled inverters in distributed generation microgrids. *IEEE Transactions on Power Electronics*, 23(6):2806–2816, Nov 2008.

[19] Seydali Ferahtia, Ali Djerioui, Hegazy Rezk, Aissa Chouder, Azeddine Houari, and Mohamed Machmoum. Adaptive droop based control strategy for dc microgrid including multiple batteries energy storage systems. *Journal of Energy Storage*, 48:103983, 2022.

[20] Sanghita Baidya and Champa Nandi. A comprehensive review on dc microgrid protection schemes. *Electric Power Systems Research*, 210:108051, 2022.

[21] G. C. Konstantopoulos and Q. C. Zhong. Nonlinear control of dc/dc power converters with inherent current and power limitation. In *2016 24th Mediterranean Conference on Control and Automation (MED)*, pages 949–954, June 2016.

[22] A.-C. Braitor, G.C. Konstantopoulos, and V. Kadirkamanathan. Admittance matrix computation and stability analysis of droop controlled DC micro-grids with CPL. *IFAC-PapersOnLine*, 53(2):13525–13530, 2020. 21th IFAC World Congress.

[23] Josep M. Guerrero, Poh Chiang Loh, Tzung-Lin Lee, and Mukul Chandorkar. Advanced control architectures for intelligent microgrids—part ii: Power quality, energy storage, and ac/dc microgrids. *IEEE Transactions on Industrial Electronics*, 60(4):1263–1270, 2013.

[24] Pulkit Nahata, Raffaele Soloperto, Michele Tucci, Andrea Martinelli, and Giancarlo Ferrari-Trecate. A passivity-based approach to voltage stabilization in dc microgrids with zip loads. *Automatica*, 113:108770, 2020.

[25] Li Xinhua, Sun Kaijun, and Li Feng. General optimal design of solar-powered unmanned aerial vehicle for priority considering propulsion system. *Chinese Journal of Aeronautics*, 33(8):2176–2188, 2020.

[26] Prakash Prashanth, Raymond L. Speth, Sebastian D. Eastham, Jayant S. Sabnis, and Steven R. H. Barrett. Post-combustion emissions control in aero-gas turbine engines. *Energy Environ. Sci.*, 14:916–930, 2021.

[27] Zhangjie Liu, Mei Su, Yao Sun, Xin Zhang, Xiao Liang, and Minghui Zheng. A comprehensive study on the existence and stability of equilibria of dc-distribution networks with constant power loads. *IEEE Transactions on Automatic Control*, 67(4):1988–1995, 2022.

[28] Andrei-Constantin Braitor and George C. Konstantopoulos. On the existence and uniqueness of equilibria in meshed dc microgrids with cpls. In *2022 30th Mediterranean Conference on Control and Automation (MED)*, pages 1030–1035, 2022.

[29] George C. Konstantopoulos and Pablo R. Baldivieso-Monasterios. State-limiting PID controller for a class of nonlinear systems with constant uncertainties. *International Journal of Robust and Nonlinear Control*, 2019.

[30] Q. C. Zhong. Robust droop controller for accurate proportional load sharing among inverters operated in parallel. *IEEE Transactions on Industrial Electronics*, 60(4):1281–1290, April 2013.

[31] John W. Simpson-Porco, Florian Dörfler, and Francesco Bullo. Voltage collapse in complex power grids. *Nature Communications*, 7(1):10790, 2016.

[32] Daniele Zonetti, Romeo Ortega, and Abdelkrim Benchaib. Modeling and control of hvdc transmission systems from theory to practice and back. *Control Engineering Practice*, 45:133–146, 2015.

[33] Andrei-Constantin Braitor, George Konstantopoulos, and Visakan Kadirkamanathan. Stability analysis of dc micro-grids with cpls under novel decentralized primary and distributed secondary control. *Automatica*, 139:110187, 2022.

[34] M. Xia, P. J. Antsaklis, V. Gupta, and M. J. McCourt. Determining passivity using linearization for systems with feedthrough terms. *IEEE Transactions on Automatic Control*, 60(9):2536–2541, 2015.

[35] Online - HelioClim Archives - Solar Radiation Data (SoDa), 2023, https://www.soda-pro.com/soda-products/hc3-archives.

[36] John A. Duffie and William A. Beckman. *System Thermal Calculations*, chapter 10, pages 422–446. John Wiley and Sons, Ltd, 2013.